

Unsteady fluid–structure interactions in a soft-walled microchannel: A one-dimensional lubrication model

Tanmay C. Inamdar and Ivan C. Christov*

School of Mechanical Engineering, Purdue University, West Lafayette, Indiana 47907, USA

(Dated: May 16, 2022)

We develop a one-dimensional model for the transient (unsteady) fluid–structure interaction (FSI) between a soft-walled microchannel and viscous fluid flow within it. An Euler–Bernoulli beam equation, which accounts for both transverse bending rigidity and nonlinear axial tension, is coupled to a one-dimensional fluid model obtained from depth-averaging the two-dimensional incompressible Navier–Stokes equations across the channel height. Specifically, the Navier–Stokes equations are scaled in the viscous (lubrication) limit relevant to microfluidics. The resulting set of coupled nonlinear partial differential equations is solved numerically through a segregated approach employing fully-implicit time stepping and second-order finite-difference discretizations. Internal FSI iterations and under-relaxation are employed to handle the stiff nonlinear algebraic problems within each time step. The Strouhal number is fixed at unity, while the Reynolds number Re and a dimensionless Young’s modulus Σ are varied independently to explore the unsteady FSI behaviors in this parameter space. A critical Re is defined by determining when the maximum steady-state deformation of the microchannel’s soft wall exceeds a certain *a priori* threshold. Our numerical results suggest that this critical Re scales as $\Sigma^{3/4}$, which is associated with “wall modes.” Furthermore, the maximum wall displacement at steady state is shown to correlate with a single dimensionless group, namely $Re/\Sigma^{0.9}$, independently of whether we consider pure bending or both bending and tension. Finally, the linear stability of the final (inflated) microchannel shape is assessed via an eigenvalue analysis, showing the existence of many marginally stable modes, which further highlights the computational challenge of simulating unsteady FSIs.

I. INTRODUCTION

Microfluidics is the part of fluid mechanics that deals with flows at small scales, on the order of microns, wherein the small dimensions, and the resulting confinement of the system, start to affect the flow physics [1]. Microfluidic flows are characterized by small geometric scales (say, h_{0f} transverse to the flow), which under normal flow conditions (velocity scale U , kinematic viscosity ν and density ρ_f) correspond to a very small Reynolds number, $Re \equiv Uh_{0f}/\nu \ll 1$. In principle, aside from giving rise to attractive academic research problems, microdevices are important as they can be used in micro total analysis systems (μ TAS) designed to perform the tests and assays, currently done with macroscale laboratory tools, but using smaller amount of working fluids at lower costs, more efficiently, and, eventually, with higher accuracy [2–4]. Therefore, microfluidics is transforming many applications, including biomedical devices, chemical processing, and thermal cooling, to name a few. For example, in the field of medical technology, microfluidics has enabled the development of a whole new field of science and technology known as *lab-on-a-chip* [5]. The latter has, in the last decade, given rise to *organ-on-a-chip* technologies [6] with the advent of biocompatible materials for microfluidic applications. Consequently, there is now significant interest in understanding unsteady fluid–structure interactions (FSIs) between low Re flows and compliant (elastic) boundaries in these contexts. Similarly, the dynamics of lubricated elastic sheets [7, 8] have broad relevance to micro-electro-mechanical systems (MEMS) design [9] and the study of complex mechanical instabilities [10]. Recently, harnessing viscous FSIs, a method of controlling soft robotic actuators using pressure forces generated by flow in an embedded microfluidic channel is being explored for different motion and actuation strategies [11, 12].

Several methods of manufacturing microfluidic devices, such as soft lithography [13] and additive or subtractive manufacturing (e.g., 3D printing) [14, 15] have emerged over the last few decades [1]. The availability of new polymer-based materials and processes, such as ink jet printing [16], has made it possible to manufacture complex geometries with relative ease, at low cost, and with high through-put [17]. For example, polydimethylsiloxane (PDMS) is a silicon-based polymeric material that is often used in manufacturing of micro-devices [18]. PDMS can be cured in layers, which allows for manufacturing of complicated geometries via casting [19]. The rheological properties of PDMS can be controlled by mixing different concentrations of the constituent polymeric substances [20], which allows for control of the compliance of soft microchannels [21].

* Author to whom correspondence should be addressed.; christov@purdue.edu; <http://tmnt-lab.org>

Microfluidic devices handle very small volumes of fluids, in the range of nano to microliters [22]. Various inventive techniques such as imposing an electric field, acoustic streaming, capillary forces, and fluid–structure interactions are required to transport fluids at the microscale [23]. However, when a fluid is pumped through a microfluidic channel, the viscous stresses at such small geometric scales result in significant pressure drops, even for very low flow rates [24]. Consequently, when this pressure drop acts against a compliant wall, it causes appreciable deformation of the microchannel [25–28]. This deformation in turn affects the flow profile and the pressure drop, which again changes the deformation of the wall, and this cycle continues thus forming the feed-back loop of FSI [29]. At vanishing Re , microchannels deform to a well-defined steady state. At finite Re , however, the coupled problem can destabilize, leading to high-frequency vibrations of the soft wall and subsequent laminar-to-turbulent transition of the flow [21, 30, 31]. Likewise, in biophysiological contexts, a weakened portion of a blood vessel (e.g., an artery, see also [32]) is known to exhibit lateral wall vibrations [33], which can lead to deadly aortic dissections [34].

The widespread use of PDMS in microfluidics makes the task of understanding the transient response of a soft channel wall due to the fluid flow underneath (and its subsequent effect on the flow itself) accessible experimentally. In fact, this inherent softness has been recently exploited to create mechanically active heart-on-a-chip devices being capable of mimicking biophysiological FSI [35]. At the same time, if most lab-on-a-chip devices are fabricated from PDMS, it is important to understand the fundamental physics of unsteady FSIs in order to be able to effectively design microfluidic systems, though few studies have done so. For example, Dendukuri et al. [36] studied the unsteady FSI problem that might arise during *stop-flow lithography*. Specifically, they were interested in the dependence of the characteristic response time, τ_r , of a soft microchannel wall on the various system parameters. Through a scaling argument for the elastic response of PDMS (applied stress p/E and wall strain ε_y proportional: $\varepsilon_y \propto p/E$) with a $Re \rightarrow 0$ lubrication fluid model, they found that $\tau_r \propto \mu \ell^2 w / (E h_{0f}^3)$, where E is the Young’s modulus of PDMS, w is the width of the channel, μ is the viscosity of the working fluid, ℓ is the flow-wise length of the channel, and h_{0f} is the initial undeformed height of the channel. The τ_r scaling is only valid for small deformation, and it cannot predict the response time *a priori*, since the constant of proportionality is unknown in this approach. Clearly, there is much to be understood about unsteady microchannel FSIs.

In parallel, the effect of instabilities in such coupled flow–compliant wall problems has been studied extensively in the high-Reynolds-number regime [37–39] but not as much in the low-Reynolds-number regime [40]. Wall-mode insatiabilities in the coupled problem can lead to efficient mixing in microchannels [21, 30, 31]. This effect can have significant implications for microfluidic technologies, as previously only diffusion and certain features of periodic laminar flows (“chaotic mixing” [41]) were thought to achieve mixing in viscous flows at the microscale [23, 42]. More importantly, this instability-driven mixing takes place at Reynolds numbers that are *orders of magnitude smaller* than the Reynolds number for transitional/turbulent flow in an equivalent rigid geometry [21, 31]. This striking effect generates further interest in unsteady FSI in soft-walled microchannels, which is the subject of the present work.

Specifically, this paper is organized as follows. First, we set out to develop a one-dimensional (1D) model of fluid–structure interactions (FSIs) in flexible, soft-walled microchannels (Sect. II), which can then be made computationally tractable (Appendix A). Next, we analyze the dynamic (Sect. III) and steady state (Sect. IV) response of this model, including complex transients, and the stability of steady states (Sect. V). Of interest is the fact that microchannel walls (unlike collapsible tubes) have significant bending rigidity, thus steady-state channel deformation profiles are not flat. Conclusions and avenues for future work are discussed in Sect. VI.

II. DERIVATION OF THE 1D LUBRICATION MODEL

Consider a topologically rectangular fluid channel whose top wall is made from a soft, compliant solid. The length of the channel (in the flow-wise direction) is ℓ , while h_{0f} and h_{0s} denote the undeformed heights (in the direction perpendicular to the flow) of the fluid channel and solid wall, respectively. The positive x -direction is taken as the flow-wise direction, i.e., the fluid flows from left to right in Fig. 1. Meanwhile, the solid wall can deform in the perpendicular y -direction. The solid displacement is assumed to vary only with x , while the fluid flow is two-dimensional (2D) having both x and y velocity components each of which might depend on both x and y . In the lubrication approach described below, the fluid model will be averaged in y to yield a one-dimensional (1D) model. Thus, at the end of the derivation, x and t will be the independent variables.

A. Solid model

To take into account the mass (inertia), bending and stretching of the channel’s top wall, we use a nonlinear tension model derived on the basis of von Kármán strains [43]. The equilibrium equations [43] for a beam, along with the constitutive equations, which relate stress resultants to strains, are simplified by making the assumptions of no axial

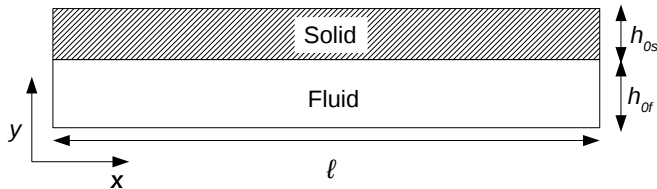


FIG. 1. Schematic of the geometry of an undeformed two-dimensional microchannel.

load, negligible axial displacement, uniform cross section and constant solid properties. It can be shown that this line of reasoning yields the following governing equation for the solid's vertical displacement u_y :

$$\rho_s \frac{\partial^2 u_y}{\partial t^2} + \frac{\partial^2}{\partial x^2} \left(EI \frac{\partial^2 u_y}{\partial x^2} \right) - \frac{3}{2} EA \left(\frac{\partial u_y}{\partial x} \right)^2 \left(\frac{\partial^2 u_y}{\partial x^2} \right) = \mathcal{L}(u_y, x, t), \quad (1)$$

where $A = wh_{0s}$ denotes the cross sectional area of the beam, ρ_s is mass per unit length of the solid, E is the Young's modulus, and I is the moment of inertia. The product EI is often termed the *bending rigidity* of the beam. The load acting on the beam in positive y -direction (i.e., from the fluid side) is denoted by \mathcal{L} .

Previous studies of FSI in three-dimensional (3D) microchannels [28, 44] have shown that deformation is bending rather than stretching dominated. In the present one-dimensional context, however, we expect large deformations and, thus, stretching of the beam. To this end, Eq. (1) removes the infinitesimal strain constraint on the ‘‘classical’’ Euler–Bernoulli beam and, thus, allows for large displacements. Finally, in this microfluidics context, the weight of the solid is assumed insignificant and gravitational forces are neglected.

The load on the solid is the result of the forces exerted by the fluid and constitutes one part of the FSI coupling. In a more general (e.g., 3D model), a full traction boundary condition is required at the fluid–solid interface. Since we are developing a 1D model, we assume that the hydrodynamic pressure p is the only force contributing to the load on the beam. (The reason for neglecting shear stresses at the fluid–solid interface is made clear in Sect. II B after making the problem dimensionless.) In Eq. (1), the load \mathcal{L} is taken as being per unit length, therefore the pressure must be multiplied by the width of the channel w (in the z -direction, out of the page as shown in Fig. 1); thus, $\mathcal{L} = wp$.

Next, Eq. (1) can be made dimensionless by choosing following dimensionless variables:

$$X = x/\ell, \quad T = t/\sqrt{\rho_s \ell^4/EI}, \quad P = p/p_0, \quad U_Y = u_y/u'_y, \quad (2)$$

where p_0 and u'_y are ‘‘dummy’’ scales for the pressure and displacement, which will be determined self-consistently as a part of the analysis. Substituting the dimensionless variables from Eq. (2) into Eq. (1) and using $\mathcal{L} = wp$ results in

$$\frac{\partial^2 U_Y}{\partial T^2} + \frac{\partial^4 U_Y}{\partial X^4} - \frac{3}{2} \frac{wh_{0s}(u'_y)^2}{I} \left(\frac{\partial U_Y}{\partial X} \right)^2 \left(\frac{\partial^2 U_Y}{\partial X^2} \right) = \frac{wp_0 \ell^4}{EI u'_y} P. \quad (3)$$

In order to couple the fluid and solid mechanics, the right-hand side of Eq. (3) must be $\mathcal{O}(1)$, which allows us to determine the characteristic vertical displacement scale self-consistently as

$$u'_y = \frac{wp_0 \ell^4}{EI}. \quad (4)$$

Substituting Eq. (4) into Eq. (3), we arrive at the dimensionless governing equation for the solid mechanics problem:

$$\frac{\partial^2 U_Y}{\partial T^2} + \frac{\partial^4 U_Y}{\partial X^4} - \alpha \left(\frac{\partial U_Y}{\partial X} \right)^2 \left(\frac{\partial^2 U_Y}{\partial X^2} \right) = P, \quad (5)$$

where α is a dimensionless tension given by

$$\alpha = \frac{3}{2} \frac{wh_{0s}(u'_y)^2}{I} = \frac{3}{2} \frac{w^3 h_{0s} p_0^2 \ell^8}{E^2 I^3}. \quad (6)$$

Note that the ultimate definition of the characteristic displacement scale u'_y will depend on the choice of fluid model and how it is nondimensionalized, through the form of p_0 to be substituted into Eq. (4).

The top wall is assumed to be clamped at both ends (the entry and exit planes of the microchannel). Hence, the relevant boundary conditions for Eq. (5) are

$$U_Y|_{X=0} = \frac{\partial U_Y}{\partial X} \Big|_{X=0} = 0, \quad U_Y|_{X=1} = \frac{\partial U_Y}{\partial X} \Big|_{X=1} = 0. \quad (7)$$

To ensure two-way coupling, we must also take into consideration the changing fluid domain. Deformed channel height is thus scaled by the undeformed channel height, and using the definition of u'_y from Eq. (4), we obtain

$$H = \frac{h}{h_{0f}} = \frac{h_{0f} + u_y}{h_{0f}} = 1 + \frac{u_y}{h_{0f}} = 1 + \frac{u'_y}{h_{0f}} U_Y = 1 + \left(\frac{wp_0 \ell^4}{EI h_{0f}} \right) U_Y. \quad (8)$$

B. Fluid model

To derive the fluid model, we start with the 2D incompressible continuity and Navier–Stokes equations [24]:

$$\frac{\partial v_x}{\partial x} + \frac{\partial v_y}{\partial y} = 0, \quad (9a)$$

$$\frac{\partial v_x}{\partial t} + v_x \frac{\partial v_x}{\partial x} + v_y \frac{\partial v_x}{\partial y} = -\frac{1}{\rho_f} \frac{\partial p}{\partial x} + \nu \left(\frac{\partial^2 v_x}{\partial x^2} + \frac{\partial^2 v_x}{\partial y^2} \right), \quad (9b)$$

$$\frac{\partial v_y}{\partial t} + v_x \frac{\partial v_y}{\partial x} + v_y \frac{\partial v_y}{\partial y} = -\frac{1}{\rho_f} \frac{\partial p}{\partial y} + \nu \left(\frac{\partial^2 v_y}{\partial x^2} + \frac{\partial^2 v_y}{\partial y^2} \right), \quad (9c)$$

where ρ_f is the fluid's density, and ν is its kinematic viscosity. The planar velocity field is denoted $\mathbf{v} = (v_x, v_y)$, where both v_x and v_y can depend on x , y and t . Next, we introduce the following dimensionless variables:

$$X = x/\ell, \quad Y = y/h_{0f}, \quad T = t / \sqrt{\rho_s \ell^4 / EI}, \quad V_X = v_x / (q_0 / h_{0f}), \quad V_Y = v_y / (\epsilon q_0 / h_{0f}), \quad P = p/p_0, \quad (10)$$

where $\epsilon \equiv h_{0f}/\ell$ is the aspect ratio of the fluid region, and q_0 is the inlet flow rate. The scales chosen for x , t and p are consistent with the ones used for solid model. Specifically, we must use the same time scale for both the fluid and solid model to ensure a two-way coupled FSI system. The scales chosen for the fluid velocity are necessary to maintain the leading-order balance in the continuity equation. Substituting the dimensionless variables from Eq. (10) into Eqs. (9) results in

$$\frac{\partial V_X}{\partial X} + \frac{\partial V_Y}{\partial Y} = 0, \quad (11a)$$

$$\frac{h_{0f}^2}{\nu \sqrt{\rho_s \ell^4 / EI}} \frac{\partial V_X}{\partial T} + \frac{q_0 h_{0f}}{\nu \ell} V_X \frac{\partial V_X}{\partial X} + \frac{\epsilon q_0}{\nu} V_Y \frac{\partial V_X}{\partial Y} = -\frac{p_0 h_{0f}^3}{\rho_f \nu q_0 \ell} \frac{\partial P}{\partial X} + \left(\frac{h_{0f}^2}{\ell^2} \frac{\partial^2 V_X}{\partial X^2} + \frac{\partial^2 V_X}{\partial Y^2} \right), \quad (11b)$$

$$\frac{\epsilon h_{0f}^2}{\nu \sqrt{\rho_s \ell^4 / EI}} \frac{\partial V_Y}{\partial T} + \frac{\epsilon q_0 h_{0f}}{\nu \ell} V_X \frac{\partial V_Y}{\partial X} + \frac{\epsilon^2 q_0}{\nu} V_Y \frac{\partial V_Y}{\partial Y} = -\frac{p_0 h_{0f}^2}{\rho_f \nu q_0} \frac{\partial P}{\partial Y} + \left(\frac{\epsilon h_{0f}^2}{\ell^2} \frac{\partial^2 V_Y}{\partial X^2} + \epsilon \frac{\partial^2 V_Y}{\partial Y^2} \right). \quad (11c)$$

Now, consider the coefficient of the time derivative in Eq. (11b):

$$\frac{h_{0f}^2}{\nu \sqrt{\rho_s \ell^4 / EI}} = \frac{q_0}{\nu} \frac{h_{0f}^2 / q_0}{\sqrt{\rho_s \ell^4 / EI}} = \frac{q_0}{\nu} \frac{h_{0f}^2}{\ell^2} \sqrt{\frac{EI}{\rho_s q_0^2}} = \epsilon Re St, \quad (12)$$

where Re is the Reynolds number defined based on the inlet flow rate, $Re \equiv q_0/\nu$, and St is the Strouhal number defined as $St \equiv \epsilon \sqrt{EI/\rho_s q_0^2}$. While the Reynolds number quantifies the balance between inertial and viscous forces, the Strouhal number (see, e.g., [24, p. 351]) is the ratio of a characteristic solid time scale ($\tau_s \sim \sqrt{\rho_s \ell^4 / EI}$) to a characteristic fluid time scale ($\tau_f \sim \ell h_{0f} / q_0$). To make the pressure gradient in Eq. (11b) a $\mathcal{O}(1)$ term, we must set

$$p_0 = \frac{\rho_f \nu q_0 \ell}{h_{0f}^3}. \quad (13)$$

Thus, our approach for the nondimensionalization of Eqs. (9) is similar to the one outlined by Stewart et al. [45], *however*, we have used a low-Reynolds formulation [viscous pressure scale, i.e., Eq. (13)] while Stewart et al. [45] used a high-Reynolds number nondimensionalization (inertial pressure scale).

Next, as it is typical of microchannels, the assumption of a long and shallow geometry is made, which means that $h_{0f} \ll w \ll \ell$ (see, e.g., the discussion in [28]). In other words, $\epsilon \equiv h_{0f}/\ell \ll 1$. Thus, all higher powers of ϵ can be dropped in the dimensionless Navier–Stokes equations. Nevertheless, we do not need to make the assumption of $Re \ll 1$. Therefore, terms of order ϵRe are allowed to be $\mathcal{O}(1)$, as in standard lubrication theory [17, 24]. Consequently, our dimensionless governing equations [i.e., Eqs. (11)] for the fluid become

$$\frac{\partial V_X}{\partial X} + \frac{\partial V_Y}{\partial Y} = 0, \quad (14a)$$

$$\epsilon Re St \frac{\partial V_X}{\partial T} + \epsilon Re V_X \frac{\partial V_X}{\partial X} + \epsilon Re V_Y \frac{\partial V_X}{\partial Y} = -\frac{\partial P}{\partial X} + \frac{\partial^2 V_X}{\partial Y^2}, \quad (14b)$$

$$\frac{\partial P}{\partial Y} = 0. \quad (14c)$$

Finally, note that in our 2D Newtonian fluid model, the only non-trivial component of the shear stress is τ_{xy} [24], which can be made dimensionless to yield a scale for the shear stress: $\tau_0 = \mu q_0/h_{0f}^2 = \epsilon p_0$. Therefore, we draw the usual conclusion that shear forces from the fluid onto the solid can be neglected in comparison to the pressure load.

C. Coupled fluid–solid model

The no-slip boundary condition is enforced on both the top and bottom walls of the microchannel. In addition, a no penetration boundary condition is imposed at the bottom wall. Since the top wall moves, a kinematic boundary condition is required there [24], which takes the form

$$St \frac{\partial H}{\partial T} = V_Y|_{Y=H} \quad (15)$$

in terms of the *dimensionless* variables introduced above. Equation (15) ensures that the vertical velocity of the fluid in contact with the moving wall is equal to the vertical velocity of the wall.

Since our goal is to obtain a 1D model, the continuity Eq. (14a) and the x -momentum Eq. (14b) are integrated over the channel height. For the continuity equation, we immediately obtain

$$\frac{\partial Q}{\partial X} + St \frac{\partial H}{\partial T} = 0, \quad (16)$$

after defining the dimensionless volumetric flow rate per unit width, $Q = \int_0^H V_X dY$, and using Eq. (15) to obtain the value of V_Y at $Y = H$. Next, the non-convective terms in the x -momentum equation are re-cast in conservative form and integrated over Y to obtain

$$\epsilon Re St \frac{\partial Q}{\partial T} + \epsilon Re \frac{\partial}{\partial X} \int_0^H V_X^2 dY = -H \frac{\partial P}{\partial X} + \left. \frac{\partial V_X}{\partial Y} \right|_{Y=0}^{Y=H}, \quad (17)$$

having assumed that V_X is a continuous function (so that we can switch the order of operation between derivative and integral), applying the no slip boundary condition, and using the reduced y -momentum Eq. (14c) to deduce that $P = P(X; T)$ (so that $\partial P/\partial X$ can be treated as constant in the integration over Y).

The final step in the process of averaging over Y is to invoke the *von Kármán–Polhausen approximation*. That is, we assume a parabolic velocity profile at each cross section in the flow [45], specifically the 2D Poiseuille profile with horizontal component $v_x = 6qy(h_{0f} - y)/h_{0f}^3$ (in dimensional variables). After nondimensionalization, $V_X = 6QY(H - Y)/H^3$ [the corresponding V_Y can be found via Eq. (14a)], and this expression can be used to evaluate the integral on the left-hand side and the last term on the right-hand side of Eq. (17) to yield

$$\epsilon Re St \frac{\partial Q}{\partial T} + \epsilon Re \frac{6}{5} \frac{\partial}{\partial X} \left(\frac{Q^2}{H} \right) = -H \frac{\partial P}{\partial X} - \frac{12Q}{H^2}. \quad (18)$$

Thus, Eqs. (16) and (18) are the final dimensionless governing equations of the fluid mechanics problem.

As mentioned above, to ensure two-way coupling, one final equation is required to close the coupling between the solid and the fluid. Now, substituting the pressure scale from Eq. (13) into the dimensionless deformed channel height in Eq. (8), we obtain

$$H = 1 + \left(\frac{\varrho_f \nu q_0 w \ell^5}{EI h_{0f}^4} \right) U_Y = 1 + \beta U_Y, \quad (19)$$

where β can be termed the *FSI parameter* because it combines *all* the fluid, solid and geometrical properties of the given setup. Specifically, we have defined

$$\beta \equiv \frac{\varrho_f \nu q_0 w \ell^5}{EI h_{0f}^4} = \frac{q_0 / \nu}{EI / (\varrho_f \nu^2 h_{0f}^2)} \frac{w \ell^5}{h_{0f}^6} = \frac{Re}{\Sigma} \frac{w \ell^5}{h_{0f}^6}. \quad (20)$$

Note that, in Eq. (20), we were able to re-write the FSI parameter β in terms of the Reynolds number $Re \equiv q_0 / \nu$ (representing the fluid's contribution), the dimensionless bending rigidity $\Sigma \equiv EI / (\varrho_f \nu^2 h_{0f}^2)$ [46] (representing the solid's contribution), and a remaining factor that is a combination of the geometric length scales. Equation (19) also forms the second part of the two-way fluid–solid coupling and performs the job of transferring solid displacements into the change of shape of microchannel.

D. Summary of the 1D Model

Equations (5), (16), (18) and (19) all-together form the coupled system of governing equations for our 1D viscous FSI problem. The key dimensionless groups are

$$\epsilon = \frac{h_{0f}}{\ell}, \quad Re = \frac{q_0}{\nu}, \quad St = \epsilon \sqrt{\frac{EI}{\varrho_s q_0^2}}, \quad \beta = \frac{\varrho_f \nu q_0 w \ell^5}{EI h_{0f}^4}. \quad (21)$$

Additionally, initial and boundary conditions are required to fully specify the problem.

The initial conditions are those of uniform flow under an undeformed wall:

$$Q|_{T=0} = 1, \quad U_Y|_{T=0} = 0 \quad \Leftrightarrow \quad H|_{T=0} = 1. \quad (22)$$

An initial inlet flow rate must be imposed, which is used to define the characteristic scales. Therefore, consistent with the von Kármán–Polhausen approximation, the flow rate everywhere in the channel ($0 \leq X \leq 1$) is initially (at time $T = 0$) set equal to the dimensionless inlet flow rate, leading to the first condition in Eq. (22). No initial conditions can be imposed on the pressure, as usual.

The boundary conditions on the solid mechanics problem are those of clamping at $X = 0$ and $X = 1$ as given in Eq. (7). The boundary conditions on the fluid mechanics problem are the imposed inlet flow rate and the outlet pressure set to gauge:

$$Q|_{X=0} = 1, \quad P|_{X=1} = 0. \quad (23)$$

Tables I and II list the typical values of dimensional system parameters (based on those summarized in [28] for 3D microchannels) and the corresponding dimensionless numbers of the FSI model. Both typical values used in experiments and modified values used for the computational examples in the present work are listed. From Table II, we observe that the value of α appears to be large compared to the other dimensionless parameters. This observation raises the possibility that terms other than the tension in Eq. (5) are negligible. However, neglecting terms besides the tension term in Eq. (5) results in a oversimplified ODE, which admits only the trivial solution $U_Y = 0$. This oversimplified ($\alpha \rightarrow \infty$) ODE is also decoupled from pressure, thus will not allow for any nontrivial deformation. On the other hand, it can be shown that combining Eq. (5) and Eq. (19) results in a PDE [see, e.g., Eq. (25)] in which the coefficient multiplying the tension term is α / β^2 , while the coefficient multiplying P is β instead of unity. All terms in this latter PDE are now the same order of magnitude. Hence, the fluid pressure has a substantial effect, even for $\alpha \gg 1$, and all the terms in Eq. (5) must be retained (even if not multiplied by α).

III. INFLATIONARY DYNAMICS OF THE MICROCHANNEL

In this section, we discuss example outcomes of unsteady FSI simulations using the model derived in Sect. II. Specifically, we address the effect of tension ($\alpha = 0$ vs. $\alpha \neq 0$), we define a critical Reynolds number and determine its scaling with other dimensionless groups, and we fit the scaling of steady-state maximum channel height and inlet pressures at steady state with the dimensionless groups Re and Σ .

Variable	Experimental value	Computational value	SI Unit
ℓ	$15,500 \times 10^{-6}$	$3,600 \times 10^{-6}$	m
h_{0s}	244×10^{-6}	55×10^{-6}	m
w	$1,700 \times 10^{-6}$	500×10^{-6}	m
E	1.6×10^6	1×10^6	Pa
ρ_s	4.025×10^{-4}	2.75×10^{-3}	kg/m
ν	1×10^{-6}	1×10^{-6}	m ² /s
ρ_f	1×10^3	1×10^3	kg/m ³
q_0	3×10^{-4}	1×10^{-6}	m ² /s
h_{0f}	244×10^{-6}	83×10^{-6}	m

TABLE I. Typical experimental and computation values of the model's dimensional parameters.

Variable	Experimental value	Computational value
ϵ	0.01574	0.02305
Re	300	1
St	0.15011	1.15757
β	39,094.191	918.953
Σ	55,306,666.666	1,006,284.173
α	27,510,403,118.386	34,617,040.380

TABLE II. Typical experimental and computation values of the model's dimensionless parameters.

A. Pure bending ($\alpha = 0$)

First, consider pure bending, the case in which tension is neglected by setting $\alpha = 0$. The following simulations show the results for $St = 1$, $Re = 50$ and $\Sigma = 1.0063 \times 10^8$. The results in this section are representative of the unsteady FSI under the model derived in Sect. II without tension. Different dimensionless numbers produce qualitatively similar result, save for changing the space and time scales.

It can be seen in Fig. 2 that the FSI reaches a steady state, after a nontrivial initial transient (from $T = 0$ to $T \approx 2$) in the fluid. The average displacement $\langle U_Y \rangle$ (over $X \in [0, 1]$), the inlet pressure $P(0, T)$ and the outlet flow rate $Q(1, T)$ all achieve steady values by the end of the simulation at $T = 10$. Specifically, the outlet flow rate $Q(1, T)$ reaches 1, which is the imposed inlet boundary condition. The steady-state values of $\langle U_Y \rangle$ and $P(0, T)$ depend in a nontrivial way on the dimensionless parameters St , Re and Σ . A video of the time evolution of the shape of the solid (specifically, the top wall), together with a reconstruction of the parabolic velocity profile under the von Kármán–Polhausen approximation is available in [47].

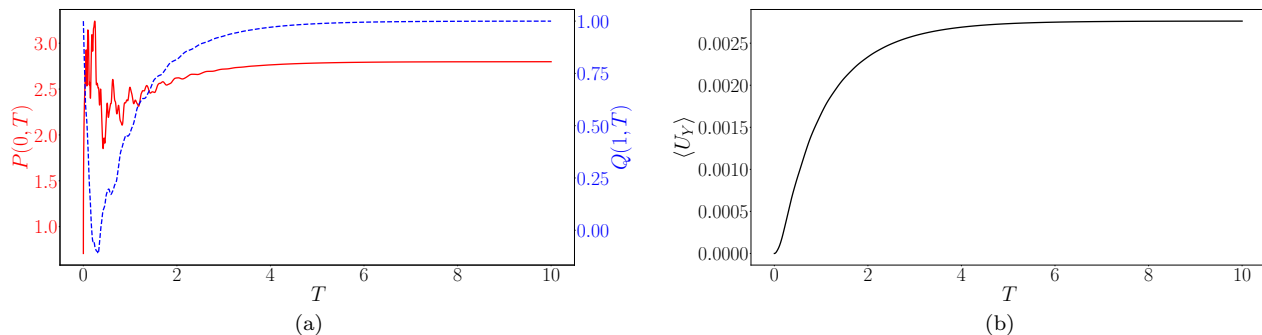


FIG. 2. (Color online) Example time histories of (a) the inlet pressure $P(0, T)$ and outlet flow rate $Q(1, T)$, and (b) the X -averaged deformation, $\langle U_Y \rangle(T) = \int_0^1 U_Y(X, T) dX$; $\alpha = 0$ and $Re = 50$.

B. Bending and tension ($\alpha \neq 0$)

Now consider the full solid model with bending and tension. In this subsection, we discuss the results for an example simulation (similar to the one considered in Sect. III A) with $St = 1$, $Re = 50$, $\Sigma = 1.0063 \times 10^8$ and $\alpha = 8.6542 \times 10^6$. Similar to the pure-bending case, the FSI reaches a steady state, as can be seen in Fig. 3, after a complex initial transient response (from $T = 0$ to $T \approx 2$) in the fluid. The final average deformation in Fig. 3b is, however, smaller than the final average deformation in Fig. 2b. This decrease is expected because, now, tension also serves to resist deformation, along with bending. As a result, the steady-state pressure value in Fig. 3a is higher than in Fig. 2a because pressure is inversely proportional to the cube of the channel height in lubrication theory, and tension is decrease the deformation (thus height). A video of the time evolution of the shape of the solid is available in [48].

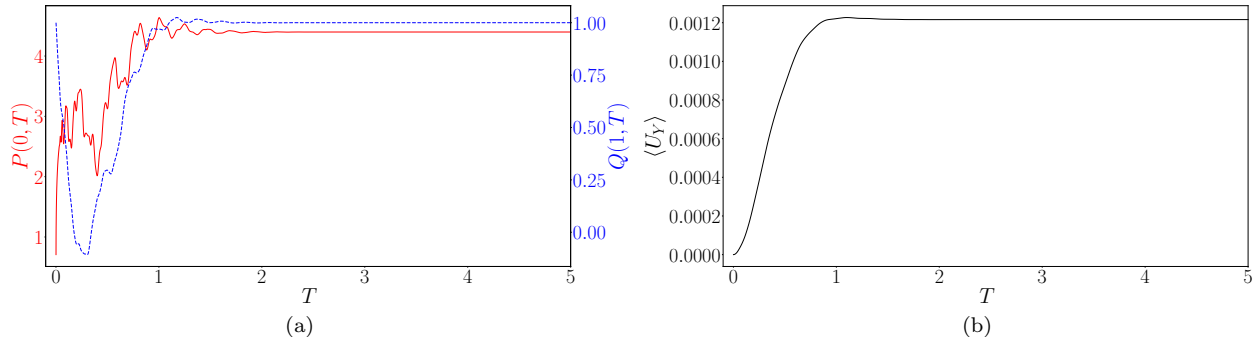


FIG. 3. (Color online) Example time histories of (a) the inlet pressure $P(0, T)$ and outlet flow rate $Q(1, T)$, and (b) the X -averaged deformation, $\langle U_Y \rangle(T) = \int_0^1 U_Y(X, T) dX$; $\alpha \neq 0$ and $Re = 50$.

C. Bending and tension at moderate Re

Since tension curbs the maximum deformation of the channel at steady state, it is reasonable to go to higher Re values, which would have produced extreme (unrealistic) deformation for $\alpha = 0$. For example, at $St = 1$, $Re = 600$ and $\Sigma = 1.0063 \times 10^8$, an interesting phenomenon is observed, as shown in Fig. 4. Before reaching a steady state, the solid passes through an intermediate state in which the outlet flow rate reaches the inlet boundary condition, i.e., $Q(1, T) = 1$ but the FSI has not equilibrated. The corresponding average deformation in Fig. 4b shows two plateaus of near constant value. During the first plateau, however, the inlet pressure continues to rise (compare to Fig. 4a). At some instant of time, the solid “snaps” into the final steady state through another, less complex, transient in the fluid. Immediately prior to to this “snap,” the inlet pressure achieves a considerably high value because the portion of the channel (near the inlet) is actually collapsed, while the portion of the channel near outlet is inflated (see Fig. 5a). Once the top wall snaps into its final steady state, inlet pressure goes down as only the middle portion of the channel is significantly inflated (see Fig. 5b). Qualitatively, the intermediate state resembles a buckling mode of a beam. Finally, we note that the pressure oscillations observed in this problems can be connected to displacement wave reflections (in the soft wall) from fixed downstream boundary as initially posited in [45], see [49].

Figure 5 shows example snapshots of the time evolution of the shape of the solid (specifically, the top wall) together with a reconstruction of the parabolic velocity profile under the von Kármán–Polhausen approximation. A video of the time evolution of the shape of the solid is available in [50].

IV. PARAMETER SCALINGS: FSI AT STEADY STATE

A. Critical Re vs. Σ Scaling

For 3D flow in a soft-walled microchannel, the critical Reynolds number, denoted Re_{crit} , is defined as the smallest Re for which the fluid flow transitions from stable laminar flow into unstable flow, or (related to the latter) flutter of the compliant channel wall is observed. This transition is marked by several changes in the fluid dynamics, such

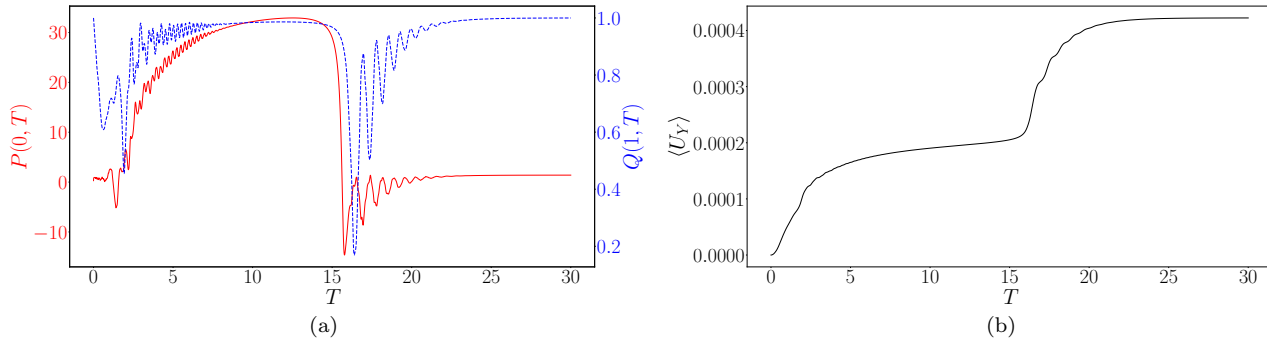


FIG. 4. (Color online) Example time histories of (a) the inlet pressure $P(0, T)$ and outlet flow rate $Q(1, T)$, and (b) the X -averaged deformation, $\langle U_Y \rangle(T) = \int_0^1 U_Y(X, T) dX$, for bending and tension ($\alpha \neq 0$) at “moderate” $Re = 600$.

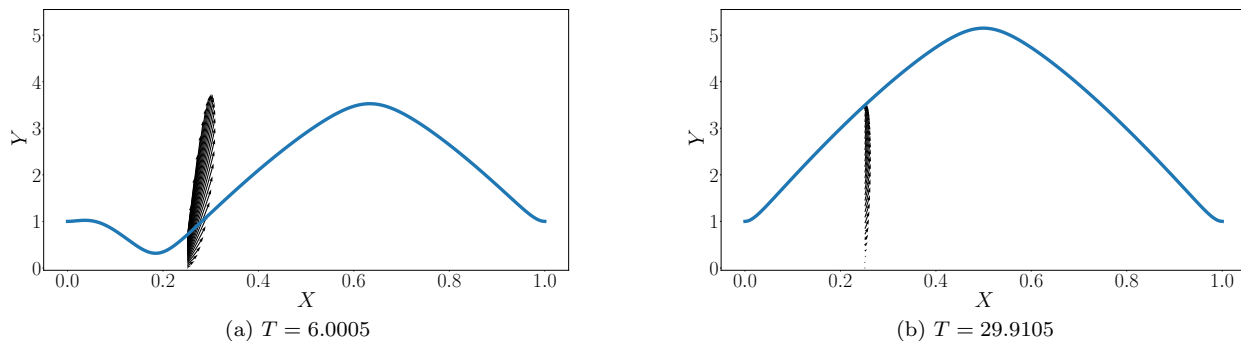


FIG. 5. Height of the deformed microchannel and an exemplar flow profile (at a specific cross-section within it, i.e., fixed X) for $\alpha \neq 0$ and moderate Re . Panel (a) shows the intermediate “buckled” state, while panel (b) shows the final inflated shape. Note that these plots are in *dimensionless* variables, hence the deflection appears exaggerated; the aspect ratio between the dimensional axes is, of course, $\epsilon \ll 1$.

as the emergence of a complex three-dimensional velocity field and improved mixing [21]. For the 1D lubrication model derived in Sect. II, it is not possible to define Re_{Crit} in the same way as in experiments because we have imposed a parabolic unidirectional velocity profile through the von Kármán–Polhausen approximation. Nevertheless, as discussed in Sect. III, the unsteady FSI response is quite complex. Consequently, finite-time numerical blow-ups (i.e., $\max_X U_Y(X, T) \rightarrow \infty$ at some finite T) are possible. However, these blow-ups are not physical instabilities, and are avoided by applying sufficient under-relaxation (i.e., by choosing a small value of ω in Appending A).

Since we cannot define Re_{Crit} in the same manner as in experiments, we must introduce an alternative definition. To this end, the value of Re for which the maximum deformation of the channel reaches ten times that of the undeformed channel height is taken as Re_{Crit} in the pure bending case ($\alpha = 0$), while five times the undeformed channel height is used for the case with nonlinear tension ($\alpha \neq 0$). Such a large deformation is not physically realistic and, thus, the flow, for the chosen Re value, that causes this amount of deformation should correspond to an unstable configuration of the fully-3D FSI problem.

It is important to note that we have explored other multipliers (beyond ten and five as discussed above), and we have verified that they have no discernible affect the scalings reported below. Furthermore, even though these criteria for how much deformation is “too much” might seem to be quite lenient (five or ten times the channel height is a large deformation indeed), it should be noted that the fluid pressure at each cross section acts on a single point instead of a cross-sectional area. The clamped boundary conditions on the side walls of a 3D model are essentially replaced by empty boundary conditions in the present 1D model. The clamped side wall boundary condition (out of the page) restricts the top wall deformation significantly in a 3D model (see, e.g., [51]). Thus, large deformations of the top wall are observed in the proposed 1D model.

Simulations across different Re values were carried out for selected Σ values, fixing $St = 1$. Figure 6a shows the

maximum height of the microchannel, after steady state has been reached, as a function of Re . Solid lines and triangles correspond to the pure-bending simulations ($\alpha = 0$), while dotted lines and squares correspond to the simulations with tension ($\alpha \neq 0$). Now, it is possible to obtain the value of the critical Reynolds number, Re_{Crit} , from Fig. 6a for a given Σ value by applying the maximum deformation criteria discussed above, for both $\alpha = 0$ and $\alpha \neq 0$. Then, $Re_{Critical}$ is plotted as a function of Σ in Fig. 6b.

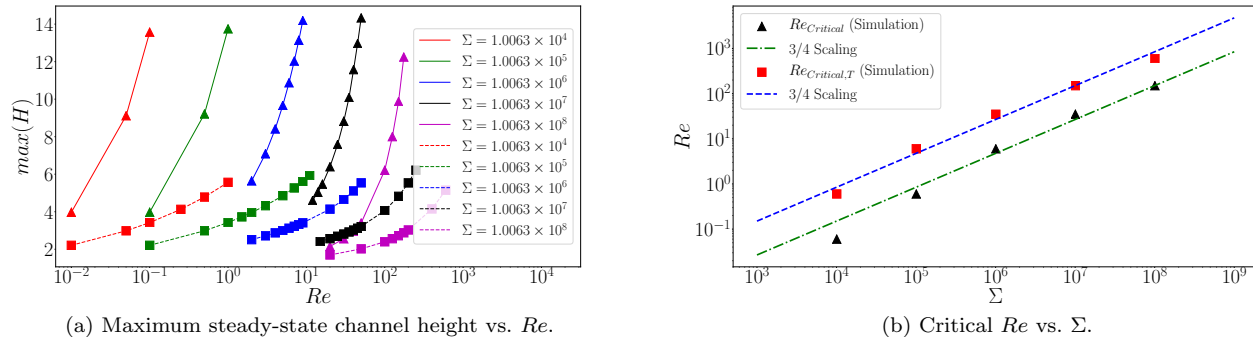


FIG. 6. (Color online) (a) Maximum height of the microchannel at steady state, $\max_{0 \leq X \leq 1} H(X, T \gg 1)$, vs. Re for different values of Σ . (b) The corresponding critical Re without tension ($\alpha = 0$, triangles) and with tension ($\alpha \neq 0$, squares) vs. Σ .

We observe, from Fig. 6b, that Re_{Crit} , for both pure bending and bending with tension, closely follows a $3/4$ scaling with respect to Σ across four decades (in both Σ and Re). Verma and Kumaran [21, 52] discussed the scaling $Re_{Crit} \propto \Sigma^{5/8}$ for transition in soft-walled microtubes and microchannels, respectively. The $5/8$ scaling is obtained from linear stability analysis of the coupled fully-3D fluid and solid mechanics by considering the changing cross-section of the flow conduit due to deformation, and it was experimentally verified (albeit over a small range of data) in [21]. However, recent experiments on microtubes do not quite support the $5/8$ scaling [53]. The scaling $3/4$ exponent is usually associated with “wall mode” instability [54–56]. Our simulations of the present 1D model show better agreement with the $3/4$ scaling, which might indicate that wall-mode instabilities are of importance in instability and transition in soft-walled microchannels, just as the experiments in [53] motivate its relevance in microtubes.

Taking a step back: Kumaran [54, 55, 57] and together with Shankar [58] carried out a number of experiments and theoretical studies on (in)stability of channel flows. Using linear stability analysis, different modes and their stability in both flexible and rigid (micro)channels and tubes at low and intermediate Reynolds numbers were analyzed. The latter work focused on either viscous modes (i.e., when there is a balance between viscous forces in the fluid and elastic forces in the solid) or inviscid modes (i.e., when there is a balance between inertial forces in fluid and elastic forces in the solid). At high Re , a boundary layer thickness of $\mathcal{O}(Re^{-1/3})$, rather than the more common Blasius laminar boundary layer thickness scaling $\mathcal{O}(Re^{-1/2})$, is observed for the inviscid modes of the FSI problem. This scaling is also characteristic of “wall modes” [55]. Specifically, for wall modes at high Re , a thin layer of vorticity forms near the wall and, thus, is affected by the stiffness (or, compliance) of the wall. Kumaran [56] suggests that these wall modes can become unstable at intermediate Re . Thus, the most surprising result of the present viscous FSI model, in which the von Kármán–Polhausen approximation prohibits any boundary layers or redistribution of vorticity across the channel height, is that the $\Sigma^{3/4}$ scaling persists. This observation might suggest that this scaling has a fundamental (intrinsic) origin in FSI problems, beyond the highly technical issues of wall mode stability [54–56].

B. Scaling of the maximum channel wall deformation

Next, we examine how the (dimensionless) maximum channel height at steady state varies with the dimensionless parameters Re and Σ . We hypothesize that it is possible to collapse the maximum channel height against a *single* dimensionless group combining Re and Σ . A plot of all the maximum heights (for both pure bending and bending with tension) vs. Re was given in Fig. 6a above. We expect that the data can be collapsed onto a single trend line by dividing Re by Σ^η , where η denotes some exponent to be determined. Specifically, Fig. 7a shows plot of the maximum deformation vs. $Re/\Sigma^{0.9}$. Filled symbols indicate the simulations for pure bending ($\alpha = 0$) and empty symbols indicates simulations for bending with tension ($\alpha \neq 0$). The trend lines shown in Fig. 7a are obtained by using the least-square algorithm to find the best fit. The coefficient of determination, R^2 , of this least-squares fit can be used to select an η for which the trend line best matches the data. Using increments of 0.1 from 0 to 1, it was found

that $\eta = 0.9$ leads to an R^2 value closest to unity for both bending and bending with tension, as shown in Fig. 7. A similar result can be obtained for the (dimensionless) inlet pressure at steady state, $P(0, T \gg 1)$, as shown in Fig. 7b, with $\eta = 0.9$ again being exponent that leads to an R^2 closest to unity. This results shows that the combined dimensionless group $Re/\Sigma^{0.9}$ captures the scaling of *both* the solid and fluid responses in our FSI problem. Note that, in dimensionless variables, the inlet pressure at steady state can be interpreted as the deformed microchannel's *hydraulic resistivity* [17], a measure of the force required to “push” fluid through it.

In both panels of Fig. 7, most of the data follows closely with the trend line, while the outliers correspond to simulations with either small Re and small Σ or large Re and large Σ . Systematic departure of the simulations corresponding to the higher Re values can be justified by noting that, at such high Re , we are “pushing” the lubrication model to the limits of its validity, thus the departure in the physics predicted. Interestingly, the best collapse of the data is obtained for the same exponent of Σ in *both* the cases of pure bending and bending with tension for both the plots of the maximum height at steady state (Fig. 7a) and the inlet pressure at steady state (Fig. 7b). The tension case does exhibit a better (“cleaner”) collapse of the data, while the simulations that start dissociating from the trend line belong to the similar part of the parameter space as in the pure-bending case. This observation indicates that even though tension does changes the particular values of height and inlet pressure, the qualitative meaning of the proposed scaling collapse remains valid for both $\alpha = 0$ and $\alpha \neq 0$. The particular significance of the 0.9 exponent remains unknown at this time, and will be the subject of future work.

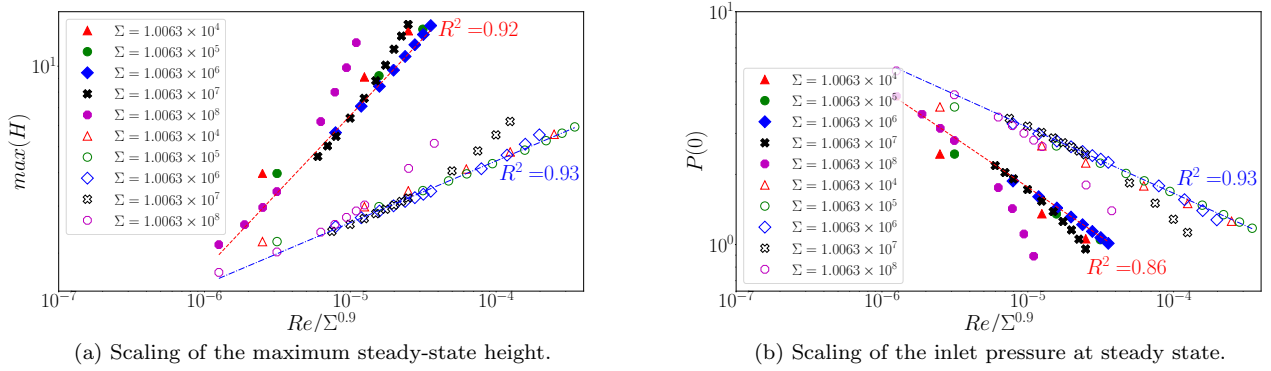


FIG. 7. (Color online) (a) Maximum steady-state deformation $\max_{0 \leq X \leq 1} H(X, T \gg 1)$ and (b) inlet pressure at steady state $P(0, T \gg 1)$, each vs. $Re/\Sigma^{0.9}$. The case without tension ($\alpha = 0$) is represented by the filled symbols, while the case with tension ($\alpha \neq 0$) is represented by the empty symbols.

V. LINEAR STABILITY OF THE STEADY-STATE MICROCHANNEL DEFORMATION

A. Steady-state microchannel shape

Having computed the transient and steady state microchannel characteristics during viscous FSI, it is worth investigating whether these shapes are truly stable against infinitesimal perturbations. To this end, we set $St = 0$ (i.e., the characteristic solid time scale is much shorter than the characteristic fluid time scale, precluding an unsteady FSI response). In this limit, Eq. (16) simply states that Q is independent of X : $\partial Q/\partial X = 0$. The flow rate is, thus, simply given by the boundary condition imposed: $Q(X, T) \equiv 1 \forall X \in [0, 1], T \geq 0$. Subsequently, Eq. (5) can be reconstituted as a PDE for H using Eq. (19). After taking an X derivative of the resulting PDE and dropping the remaining unsteady terms, we obtain a fifth-order PDE:

$$\frac{\partial^5 H}{\partial X^5} - \frac{\alpha}{\beta^2} \frac{\partial}{\partial X} \left[\left(\frac{\partial H}{\partial X} \right)^2 \left(\frac{\partial^2 H}{\partial X^2} \right) \right] = \beta \frac{\partial P}{\partial X}. \quad (24)$$

Next, Eq. (18) can be used to solve for $\partial P/\partial X$, the expression for which can then be substituted into Eq. (24):

$$\frac{\partial^5 H}{\partial X^5} - \frac{\alpha}{\beta^2} \frac{\partial}{\partial X} \left[\left(\frac{\partial H}{\partial X} \right)^2 \left(\frac{\partial^2 H}{\partial X^2} \right) \right] = \beta \left(\epsilon Re \frac{6}{5} \frac{1}{H^3} \frac{\partial H}{\partial X} - \frac{12}{H^3} \right). \quad (25)$$

This final fifth-order nonlinear PDE (25) for H can be compared to [45, Eq. (2.12a)], which was derived by Stewart et al. for H but in the high- Re context. In the model in [45], stretching is the dominant solid mechanics response and bending is neglected by assuming small deformations. Thus, [45, Eq. (2.12a)] differs from Eq. (25) in two principal ways: (i) Re only modifies the fluid inertia term in Eq. (25) while it modifies *both* the fluid inertia and the nonlinear stretching terms in [45, Eq. (2.12a)]; (ii) the higher-order bending term on the left-hand side of Eq. (25) is not present in [45, Eq. (2.12a)] and, likewise, the nonlinear stretching term on the left-hand side of Eq. (25) is to be contrasted with the linearized tension term in [45, Eq. (2.12a)]. Consequently, we expect that the steady-states governed by Eq. (25), and their linear stability, to differ significantly from those studied by Stewart et al. [45], paving the way to potentially rich new dynamic behaviors in the present viscous FSI model.

To compute the steady state channel shape, denoted $H_0(X)$, we re-interpret Eq. (25) as a two-point boundary-value problem using SciPy's `solve_bvp` subject to

$$H_0(X=0) = \left. \frac{\partial H_0}{\partial X} \right|_{X=0} = 0, \quad H_0(X=1) = \left. \frac{\partial H_0}{\partial X} \right|_{X=1} = 0, \quad \left. \frac{\partial^4 H_0}{\partial X^4} \right|_{X=1} = 0, \quad (26)$$

where the first two boundary conditions are simply the clamped conditions [see Eq. (7)], while the third is the outlet pressure condition [see Eq. (23)] rewritten in terms of the steady-state channel height via Eq. (5). The steady-state solutions computed by solving the nonlinear boundary value problem posed by Eqs. (25) and (26) compare very favorably with the dynamic simulation results. Specifically, the maximum channel heights reported in Fig. 6a agree very well with those computed from Eqs. (25) and (26).

B. Perturbation about the steady state

A detailed analysis of the linear stability of the flat-state solution of Eq. (25) could be of interest because there is a potentially rich stability diagram, similar to the one constructed in [45]. However, here we are interested in the stability of the steady state in the presence of bending and tension of the top wall, which is *not* a flat state, unlike the case of collapsible tubes [45, 59]. To understand the stability of this non-flat steady state, we perturb about $Q = 1$ and $H = H_0(X)$ [i.e., the solution of Eqs. (25) and (26)] as follows:

$$Q(X, T) = 1 + \delta Q_1(X, T), \quad (27a)$$

$$H(X, T) = H_0(X) + \delta H_1(X, T), \quad (27b)$$

where $\delta \ll 1$ is the (arbitrary, dimensionless) amplitude of a small perturbation. The fixed boundary condition at both ends are already satisfied by the steady-state solution $(Q_0 = 1, H_0)^\top$, thus the perturbation $(Q_1, H_1)^\top$ satisfies *homogeneous* boundary conditions.

To determine the growth/decay of the perturbation, we must derive a set of linear evolution equations for Q_1 and H_1 . To this end, we substitute Eqs. (27) into the governing set of Eqs. (5), (16), (18) and (19), using the fact that $H_0(X)$ satisfies Eq. (25) and dropping all terms of $\mathcal{O}(\delta^2)$ or higher. The result is two linear evolution equations in which the coefficients depend on the steady-state $H_0(X)$ and its derivatives:

$$\begin{aligned} \frac{\partial^5 H_1}{\partial X^5} - \frac{\alpha}{\beta^2} \frac{\partial}{\partial X} \left[\left(\frac{\partial H_0}{\partial X} \right)^2 \frac{\partial^2 H_1}{\partial X^2} + 2 \frac{\partial^2 H_0}{\partial X^2} \frac{\partial H_0}{\partial X} \frac{\partial H_1}{\partial X} \right] = - \frac{\partial^3 H_1}{\partial X \partial T^2} - \beta \left\{ \frac{\epsilon Re St}{H_0} \frac{\partial Q_1}{\partial T} \right. \\ \left. + \epsilon Re \frac{6}{5} \left[\frac{2H_1}{H_0^4} \frac{\partial H_0}{\partial X} - \frac{1}{H_0^3} \frac{\partial H_1}{\partial X} - \frac{2Q_1}{H_0^3} \frac{\partial H_0}{\partial X} + \frac{2}{H_0^2} \frac{\partial Q_1}{\partial X} + \frac{H_1}{H_0^4} \frac{\partial H_0}{\partial X} \right] + 12 \left(-\frac{3H_1}{H_0^4} + \frac{Q_1}{H_0^3} \right) \right\}, \quad (28a) \end{aligned}$$

$$\frac{\partial Q_1}{\partial X} + St \frac{\partial H_1}{\partial T} = 0. \quad (28b)$$

To deal with the mixed derivative on the right-hand side of Eq. (28a), we use Eq. (28b) to replace $\partial H_1 / \partial T$ with $\partial Q_1 / \partial T$ and re-arrange so that time derivatives are collected on the left-hand side:

$$\begin{aligned} \left(\beta \frac{\epsilon Re St}{H_0} - \frac{1}{St} \frac{\partial^2}{\partial X^2} \right) \frac{\partial Q_1}{\partial T} = - \frac{\partial^5 H_1}{\partial X^5} + \frac{\alpha}{\beta^2} \frac{\partial}{\partial X} \left[\left(\frac{\partial H_0}{\partial X} \right)^2 \frac{\partial^2 H_1}{\partial X^2} + 2 \frac{\partial^2 H_0}{\partial X^2} \frac{\partial H_0}{\partial X} \frac{\partial H_1}{\partial X} \right] \\ - \beta \left\{ \epsilon Re \frac{6}{5} \left[\frac{2H_1}{H_0^4} \frac{\partial H_0}{\partial X} - \frac{1}{H_0^3} \frac{\partial H_1}{\partial X} - \frac{2Q_1}{H_0^3} \frac{\partial H_0}{\partial X} + \frac{2}{H_0^2} \frac{\partial Q_1}{\partial X} + \frac{H_1}{H_0^4} \frac{\partial H_0}{\partial X} \right] + 12 \left(-\frac{3H_1}{H_0^4} + \frac{Q_1}{H_0^3} \right) \right\}. \quad (29) \end{aligned}$$

Thus, we have arrived at a first-order-in-time linear evolution problem:

$$\frac{\partial}{\partial T} \begin{pmatrix} Q_1 \\ H_1 \end{pmatrix} = \mathbf{A} \begin{pmatrix} Q_1 \\ H_1 \end{pmatrix}, \quad \mathbf{A} \equiv \begin{pmatrix} \mathcal{A}_1 & \mathcal{A}_2 \\ \mathcal{A}_3 & 0 \end{pmatrix}, \quad (30)$$

where the block operator \mathbf{A} , which involves H_0 , the dimensionless parameters (ϵ , α , β , Re , St) and various derivative operators, will determine how perturbations to a steady-state will grow/decay. The blocks can be written out in full:

$$\mathcal{A}_1 = \left(\beta \frac{\epsilon Re St}{H_0} - \frac{1}{St} \frac{\partial^2}{\partial X^2} \right)^{-1} \left(-\frac{12\beta}{H_0^3} + \frac{12\epsilon\beta Re}{5H_0^3} \frac{\partial H_0}{\partial X} - \frac{12\epsilon\beta Re}{5H_0^2} \frac{\partial}{\partial X} \right), \quad (31a)$$

$$\begin{aligned} \mathcal{A}_2 = & \left(\beta \frac{\epsilon Re St}{H_0} - \frac{1}{St} \frac{\partial^2}{\partial X^2} \right)^{-1} \left[\frac{36\beta}{H_0^4} - \frac{18\epsilon\beta Re}{5H_0^4} \frac{\partial H_0}{\partial X} + \frac{6\epsilon\beta Re}{5H_0^3} \frac{\partial}{\partial X} + \frac{2\alpha}{\beta^2} \left(\frac{\partial^2 H_0}{\partial X^2} \right)^2 \frac{\partial}{\partial X} \right. \\ & \left. + \frac{2\alpha}{\beta^2} \frac{\partial H_0}{\partial X} \frac{\partial^3 H_0}{\partial X^3} \frac{\partial}{\partial X} + \frac{4\alpha}{\beta^2} \frac{\partial H_0}{\partial X} \frac{\partial^2 H_0}{\partial X^2} \frac{\partial^2}{\partial X^2} + \frac{\alpha}{\beta^2} \left(\frac{\partial H_0}{\partial X} \right)^2 \frac{\partial^3}{\partial X^3} - \frac{\partial^5}{\partial X^5} \right], \quad (31b) \end{aligned}$$

$$\mathcal{A}_3 = -\frac{1}{St} \frac{\partial}{\partial X}. \quad (31c)$$

Upon discretizing in space (on a grid with N_X nodes), pre-factors in the definition of \mathcal{A}_1 and \mathcal{A}_2 will be represented by matrices that can be inverted and easily applied to the remaining terms, yielding a $2N_X \times 2N_X$ block matrix \mathbf{A} .

C. Eigenspectra of the linearized operator

When discretized, Eqs. (28) do *not* give rise to an autonomous with self-adjoint matrix operator \mathbf{A} due to the non-uniform base state (see, e.g., the discussion in [60] in the context of thin-film lubrication). Therefore, issues of transient growth and non-modal analysis arise [60, 61]. For the present purposes, we are just interested in the *asymptotic* stability of the inflated steady-states, so it suffices to consider the eigenspectrum of \mathbf{A} for different parameters, as shown in Fig. 8, and determine the possibility of eigenvalues with positive real part.

Figure 8 shows eigenspectra, i.e., the set $\{\sigma \in \mathbb{C} \mid \mathbf{A}\psi = \sigma\psi, \psi \neq 0\}$, for four different combinations of Re (which directly affects β) and α . The lightly colored dots (red online) show eigenvalues σ with positive real part. However, σ with positive $\text{Re}(\sigma)$ appear to be an artifact of the numerical approximation of \mathbf{A} arising from the finite number of mesh points used in the spatial discretization. In Fig. 8, we use $N_X = 3,200$, however, we have verified numerically that the magnitude of eigenvalue with largest positive real part *decreases linearly* with N_X . Therefore, for a perfect discretization with $N_X \rightarrow \infty$, we expect that eigenvalue with largest positive real part will converge to the imaginary axis. Similarly, the eigenvalue with largest imaginary part increases with N_X and, so, its magnitude diverges with $N_X \rightarrow \infty$. Tension ($\alpha = 0$ or $\alpha \neq 0$) has only a slight effect on the eigenvalues at the edge of imaginary axis.

The presence of large number of eigenvalue near the imaginary axis suggest a neutrally stable system. This observation highlights the *stiffness* of the unsteady FSI problem. Consequently, we had to develop a robust, fully-implicit finite-difference scheme with under-relaxation, as described in Appendix A. As can be seen from the eigenspectra plots at finite spatial resolution, increasing Re causes the largest positive real part of eigenvalues to increase, and, thus, at higher Re the transient simulations become more and more difficult to run. Since, we expect that, with infinite spatial resolution for discretizing \mathbf{A} , all σ have $\text{Re}(\sigma) = 0$, and our 1D problem always reaches a steady state.

VI. CONCLUSION

In this paper, we derived a one-dimensional (1D) model for unsteady viscous fluid–structure interactions (FSIs) starting from a two-dimensional (2D) Cartesian geometry in which an initially rectangular fluid domain contains a Newtonian fluid obeying the Navier–Stokes equations, while the top boundary of the geometry is a beam of finite thickness that supports both bending and nonlinear tension. The parameter space of this model was shown to consist of a Reynolds number Re , a Strouhal number St , a dimensionless elastic modulus Σ , the channel aspect ratio ϵ , a dimensionless FSI coupling parameter β (which was re-expressed in terms of Re , Σ and the channel dimensions), and a dimensionless nonlinear tension α . Fixing ϵ and St , we explored the effect of α , Re and Σ on unsteady FSIs.

Specifically, with our reduced-order 1D model in hand, we sought to substantiate previously derived scaling relations between Re and Σ near the threshold of instability. By constructing a strongly implicit finite difference scheme for our 1D FSI model, we were able to explore the nontrivial transient response of viscous microchannel FSIs. Specifically, by

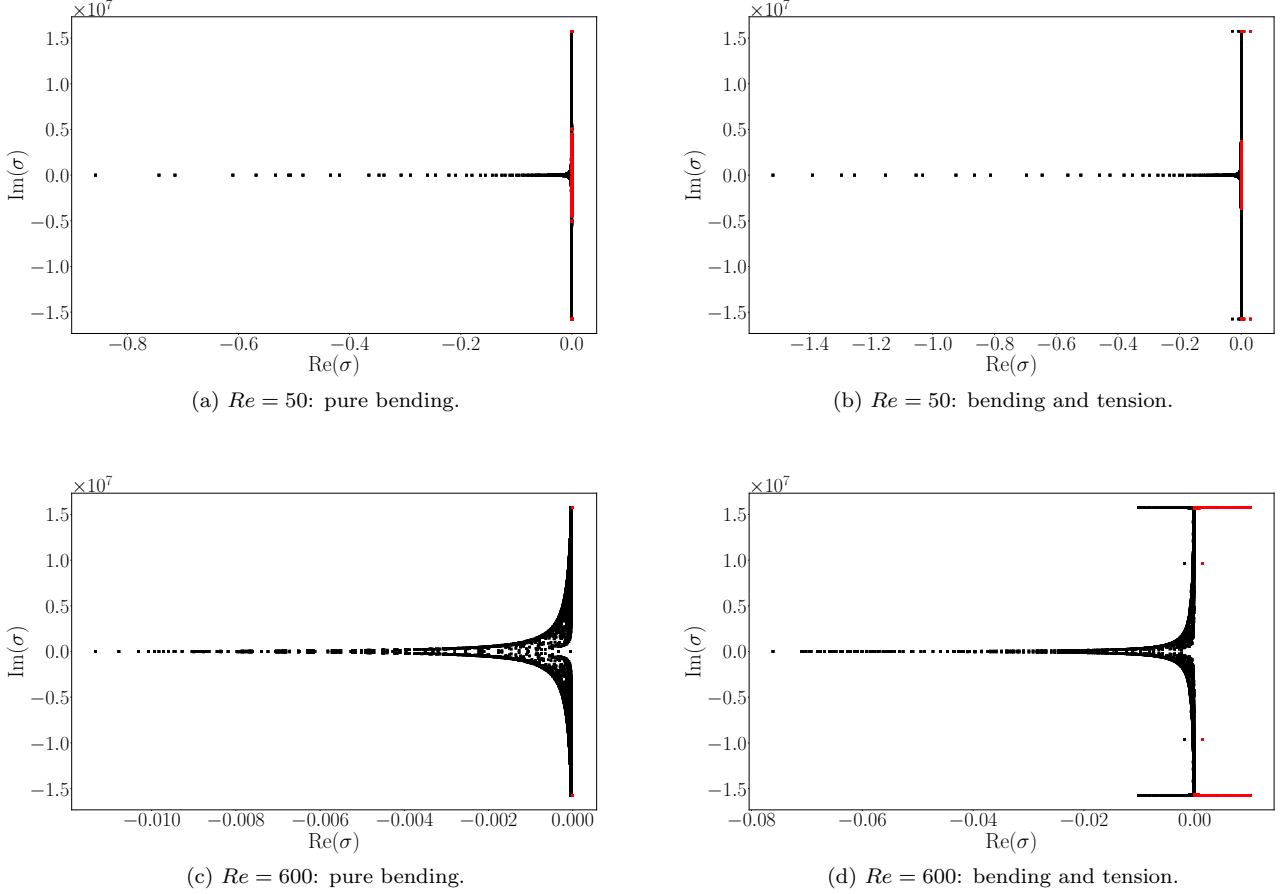


FIG. 8. (Color online) Eigenspectra, in the complex plane \mathbb{C} , of the discretized linear operator \mathbf{A} . Dots indicate individual eigenvalues; lightly colored ones indicate eigenvalues with $\text{Re}(\sigma) > 0$.

setting a criterion for when the maximum steady-state deformation exceeds some multiple of the initial microchannel height, we determined a “critical” Reynolds number and showed that it scales as $Re_{\text{critical}} \propto \Sigma^{3/4}$ across four decades of each. Our finding, based on a reduced order model, highlights the complexity of unsteady FSIs at the microscale and further motivates the need for research into modes of instability in such coupled problems. Furthermore, through extensive numerical simulations, we concluded that nonlinear tension (as quantified by α) does not change the qualitative response (as seen in Fig. 7) but only affects pre-factors in the scaling.

To highlight novel aspects of scaling the governing equations in the viscous (lubrication) limit, we addressed some exemplar coupled flow–deformation behaviors through our numerical simulations. Specifically, at moderate Re in the presence of nonlinear tension, an intermediate almost-stable state, which resembles a beam’s buckling mode, exists. This observation is consistent with the fact that nonlinear tension could allow for multiple steady-state solution of the problem for the same (clamped) boundary conditions. Nevertheless, the intermediate “buckled” state observed is not one of the solution admitted by the steady-state problem, therefore this is a distinct, purely transient, effect.

We showed that the maximum steady-state channel height (a way to quantify the solid mechanics response) and the inlet pressure (a way to quantify the fluid mechanics response) at steady state can *both* be collapsed (to a large extent) against the combination of dimensionless groups given by $Re/\Sigma^{0.9}$. This observation suggest that possibility of *universality* in the scaling laws for microchannel FSIs. Unfortunately, the exponent 0.9 came from a fitting procedure and not from dimensional analysis (or scaling). Uncovering its significance will be the subject of future work.

The present work is a complementary line of inquiry to Pedley’s collapsible tubes research program (see, e.g., [62, 63]) in which reduced-order (typically, 1D) models have been derived for biophysiological FSIs under the boundary-layer (high Re) scaling of the Navier–Stokes equations. The main difference between the latter and our present work is that we have scaled the Navier–Stokes equations in the lubrication limit relevant to microfluidics, which changes the relative “importance” of various flow effects on the coupled FSI problem. Our work is also distinct from previous FSI

models in which *inviscid* flow is coupled to a nonlinear beam with stretching and rotation [64, 65] or to a nonlinear von Kármán plate [66]. Nevertheless, it would be worthwhile generalizing the mathematical techniques and stability results obtained in [64, 66] to the present *viscous* context. Microscale unsteady FSI with non-Newtonian fluid rheology, e.g., shear-rate-dependent viscosity [67], is another avenue of future research. Furthermore, it would also be of interest to explore geometric effects: cylindrical vs. Cartesian geometries (see, e.g., [67–69]), however the cylindrical case requires a wholly different elasticity model. It might also be prudent to take capillary effects into account during *unsteady* microscale FSI, building upon the steady case [70] and prior work on *elastocapillarity* [71].

Finally, there are a number of distinguished limits of our model that would be of interest to analyze in future work. These limiting models are discussed in [49], and here we briefly summarize just the most important limits. Specifically, the limits of $St \rightarrow 0$ and $St \rightarrow \infty$ correspond to physical situations in which either the solid time scale or the fluid time scale, respectively, dominates the physics completely. Consequently, in each of these limits, the unsteady effects in the other medium are negligible. Since either the solid mechanics strongly affects the fluid mechanics or vice versa, in $St \rightarrow 0$ and $St \rightarrow \infty$ limits respectively, then in each limit one of the mechanical problems is assumed to be “subjugated” to the other, leading to something akin to weakly-coupled *one-way* FSI. A similar discussion regarding the comparison between fluid and solid time scales can be found in [11].

ACKNOWLEDGMENTS

We thank V. Anand, F. Municchi and T. C. Shidhore each for a critical reading of the manuscript and helpful suggestions. This research was supported, in part, by the US National Science Foundation under grant No. CBET-1705637.

-
- [1] N.-T. Nguyen and S. T. Wereley, *Fundamentals and Applications of Microfluidics*, 2nd ed., Integrated Microsystems Series (Artech House, Norwood, MA, 2006).
 - [2] D. R. Reyes, D. Iossifidis, P.-A. Auroux, and A. Manz, “Micro total analysis systems. 1. Introduction, theory, and technology,” *Anal. Chem.* **74**, 2623–2636 (2002).
 - [3] P.-A. Auroux, D. Iossifidis, D. R. Reyes, and A. Manz, “Micro total analysis systems. 2. Analytical standard operations and applications,” *Anal. Chem.* **74**, 2637–2652 (2002).
 - [4] J. M. Bienvenue, J. Karlinsey, J. P. Landers, and J. P. Ferrance, “Clinical Applications of Microfluidic Devices,” in *Electrokinetic Phenomena: Principles and Applications in Analytical Chemistry and Microchip Technology*, edited by A. S. Rathore and A. Guttman (Marcel Dekker, Inc., New York, 2004) Chap. 15, pp. 427–469.
 - [5] S. Chakraborty, ed., *Microfluidics and Microscale Transport Processes*, IIT Kharagpur Research Monograph Series (CRC Press, Boca Raton, FL, 2013).
 - [6] D. Huh, B. D. Matthews, A. Mammoto, M. Montoya-Zavala, H. Y. Hsin, and D. E. Ingber, “Reconstituting organ-level lung functions on a chip,” *Science* **328**, 1662–1668 (2010).
 - [7] A. E. Hosoi and L. Mahadevan, “Peeling, healing, and bursting in a lubricated elastic sheet,” *Phys. Rev. Lett.* **93**, 137802 (2004).
 - [8] I. J. Hewitt, N. J. Balmforth, and J. R. De Bruyn, “Elastic-plated gravity currents,” *Eur. J. Appl. Math.* **26**, 1–31 (2015).
 - [9] C.-M. Ho and Y.-C. Tai, “Micro-electro-mechanical-systems (MEMS) and fluid flows,” *Annu. Rev. Fluid Mech.* **30**, 579–612 (1998).
 - [10] A. Juel, D. Pihler-Puzović, and M. Heil, “Instabilities in blistering,” *Annu. Rev. Fluid Mech.* **50**, 691–714 (2018).
 - [11] Y. Matia, T. Elimelech, and A. D. Gat, “Leveraging internal viscous flow to extend the capabilities of beam-shaped soft robotic actuators,” *Soft Robotics* **4**, 126–134 (2017).
 - [12] E. Boyko, A. D. Gat, and M. Bercovici, “Deformations of a pre-stretched and lubricated finite elastic sheet,” preprint, arXiv:1703.06820 (2018).
 - [13] Y. Xia and G. M. Whitesides, “Soft Lithography,” *Annu. Rev. Mater. Sci.* **28**, 153–184 (1998).
 - [14] D. Therriault, S. R. White, and J. A. Lewis, “Chaotic mixing in three-dimensional microvascular networks fabricated by direct-write assembly,” *Nat. Mat.* **2**, 265–271 (2003).
 - [15] P. J. Kitson, M. H. Rosnes, V. Sans, V. Dragone, and L. Cronin, “Configurable 3D-Printed millifluidic and microfluidic ‘lab on a chip’ reactionware devices,” *Lab Chip* **12**, 3267–3271 (2012).
 - [16] W. Su, B. S. Cook, Y. Fang, and M. M. Tentzeris, “Fully inkjet-printed microfluidics: A solution to low-cost rapid three-dimensional microfluidics fabrication with numerous electrical and sensing applications,” *Sci. Rep.* **6**, 1–12 (2016).
 - [17] H. Bruus, *Theoretical Microfluidics*, Oxford Master Series in Condensed Matter Physics (Oxford University Press, Oxford, UK, 2008).
 - [18] J. C. McDonald and G. M. Whitesides, “Poly(dimethylsiloxane) as a material for fabricating microfluidic devices,” *Acc. Chem. Res.* **35**, 491–499 (2002).
 - [19] J. Friend and L. Yeo, “Fabrication of microfluidic devices using polydimethylsiloxane,” *Biomicrofluidics* **4**, 026502 (2010).

- [20] I. D. Johnston, D. K. McCluskey, C. K. L. Tan, and M. C. Tracey, “Mechanical characterization of bulk Sylgard 184 for microfluidics and microengineering,” *J. Micromech. Microeng.* **24**, 35017 (2014).
- [21] M. K. S. Verma and V. Kumaran, “A multifold reduction in the transition Reynolds number, and ultra-fast mixing, in a micro-channel due to a dynamical instability induced by a soft wall,” *J. Fluid Mech.* **727**, 407–455 (2013).
- [22] T. M. Squires and S. R. Quake, “Microfluidics: Fluid physics at the nanoliter scale,” *Rev. Mod. Phys.* **77**, 977–1026 (2005).
- [23] H. A. Stone, A. D. Stroock, and A. Ajdari, “Engineering flows in small devices: Microfluidics toward a Lab-on-a-Chip,” *Annu. Rev. Fluid Mech.* **36**, 381–411 (2004).
- [24] R. L. Panton, *Incompressible Flow*, 4th ed. (John Wiley & Sons, Hoboken, NJ, 2013).
- [25] M. A. Holden, S. Kumar, A. Beskok, and P. S. Cremer, “Microfluidic diffusion diluter: bulging of PDMS microchannels under pressure-driven flow,” *J. Micromech. Microeng.* **13**, 412–418 (2003).
- [26] T. Gervais, J. El-Ali, A. Günther, and K. F. Jensen, “Flow-induced deformation of shallow microfluidic channels,” *Lab Chip* **6**, 500–507 (2006).
- [27] M. K. Raj, S. DasGupta, and S. Chakraborty, “Hydrodynamics in deformable microchannels,” *Microfluid. Nanofluid.* **21**, 70 (2017).
- [28] I. C. Christov, V. Cognet, T. C. Shidhore, and H. A. Stone, “Flow rate–pressure drop relation for deformable shallow microfluidic channels,” *J. Fluid Mech.* **814**, 267–286 (2018).
- [29] See, e.g., Fung’s illustration [32, Figure 3.4:2] for a schematic visual representation of this FSI feed-back loop in hemoelastic system.
- [30] S. S. Srinivas and V. Kumaran, “Effect of viscoelasticity on the soft-wall transition and turbulence in a microchannel,” *J. Fluid Mech.* **812**, 1076–1118 (2017).
- [31] M. K. S. Verma and V. Kumaran, “Stability of the flow in a soft tube deformed due to an applied pressure gradient,” *Phys. Rev. E* **91**, 043001 (2015).
- [32] Y. C. Fung, *Biomechanics: Circulation*, 2nd ed. (Springer-Verlag, New York, 1997).
- [33] T. J. Pedley, *The Fluid Mechanics of Large Blood Vessels* (Cambridge University Press, Cambridge, 1980).
- [34] J. B. Grotberg and O. E. Jensen, “Biofluid mechanics in flexible tubes,” *Annu. Rev. Fluid Mech.* **36**, 121–147 (2004).
- [35] J. U. Lind, T. A. Busbee, A. D. Valentine, F. S. Pasqualini, H. Yuan, M. Yadid, S. J. Park, A. Kotikian, A. P. Nesmith, P. H. Campbell, J. J. Vlassak, J. A. Lewis, and K. K. Parker, “Instrumented cardiac microphysiological devices via multimaterial three-dimensional printing,” *Nat. Mat.* **16**, 303–308 (2017).
- [36] D. Dendukuri, S. S. Gu, D. C. Pregibon, T. A. Hatton, and P. S. Doyle, “Stop-flow lithography in a microfluidic device,” *Lab Chip* **7**, 818–828 (2007).
- [37] J. J. Riley, M. Gad-el Hak, and R. W. Metcalfe, “Complaint coatings,” *Annu. Rev. Fluid Mech.* **20**, 393–420 (1988).
- [38] M. Gad-el Hak, “Compliant coatings: A decade of progress,” *Appl. Mech. Rev.* **49**, S147–S157 (1996).
- [39] “Plates in axial flow,” in *Fluid-Structure Interactions*, Vol. 2, edited by M. P. Paidoussis (Academic Press, 2003) Chap. 10, pp. 1137–1220.
- [40] C. Duprat and H. A. Stone, eds., *Fluid-Structure Interactions in Low-Reynolds-Number Flows* (The Royal Society of Chemistry, Cambridge, UK, 2016).
- [41] J. M. Ottino, *The Kinematics of Mixing: Stretching, Chaos, and Transport*, Cambridge Texts in Applied Mathematics, Vol. 3 (Cambridge University Press, Cambridge, UK, 1989).
- [42] J. M. Ottino and S. Wiggins, “Introduction: mixing in microfluidics,” *Phil. Trans. R. Soc. A* **362**, 923–935 (2004).
- [43] J. N. Reddy, *An introduction to nonlinear finite element analysis* (Oxford University Press, Oxford, UK, 2004).
- [44] M. Gomez, D. E. Moulton, and D. Vella, “Passive control of viscous flow via elastic snap-through,” *Phys. Rev. Lett.* **119**, 144502 (2017).
- [45] P. S. Stewart, S. L. Waters, and O. E. Jensen, “Local and global instabilities of flow in a flexible-walled channel,” *Eur. J. Mech. B/Fluids* **28**, 541–557 (2009).
- [46] We use the notation Σ , which coincides with the notation in [21] and the references therein, because our definition is similar to the dimensionless solid mechanics parameter therein.
- [47] See the Supplemental Material at [URL will be inserted by publisher] for the video `z_displacement50.mp4` showing the time evolution of the shape of the solid $\alpha = 0$ and $Re = 50$.
- [48] See the Supplemental Material at [URL will be inserted by publisher] for the video `z_displacement50t.mp4` showing the time evolution of the shape of the solid $\alpha \neq 0$ and $Re = 50$.
- [49] T. C. Inamdar, *Unsteady fluid-structure interactions in soft-walled microchannels*, Master’s thesis, Purdue University, West Lafayette, Indiana (2018).
- [50] See the Supplemental Material at [URL will be inserted by publisher] for the video `z_displacement600t.mp4` showing the time evolution of the shape of the solid $\alpha \neq 0$ and $Re = 600$.
- [51] T. C. Shidhore and I. C. Christov, “Static response of deformable microchannels: a comparative modelling study,” *J. Phys.: Condens. Matter* **30**, 054002 (2018).
- [52] M. K. S. Verma and V. Kumaran, “A dynamical instability due to fluidwall coupling lowers the transition Reynolds number in the flow through a flexible tube,” *J. Fluid Mech.* **705**, 322–347 (2012).
- [53] R. Neelamegam and V. Shankar, “Experimental study of the instability of laminar flow in a tube with deformable walls,” *Phys. Fluids* **27**, 024102 (2015).
- [54] V. Kumaran, “Stability of the flow of a fluid through a flexible tube at intermediate Reynolds number,” *J. Fluid Mech.* **357**, 123–140 (1998).
- [55] V. Kumaran, “Asymptotic analysis of wall modes in a flexible tube,” *Eur. Phys. J. B* **4**, 519–527 (1998).
- [56] V. Kumaran, “Stability of wall modes in a flexible tube,” *J. Fluid Mech.* **362**, 1–15 (1998).

- [57] V. Kumaran, “Stability of the viscous flow of a fluid through a flexible tube,” *J. Fluid Mech.* **294**, 259–281 (1995).
- [58] V. Shankar and V. Kumaran, “Stability of non-parabolic flow in a flexible tube,” *J. Fluid Mech.* **395**, 211–236 (1999).
- [59] P. S. Stewart, “Instabilities in flexible channel flow with large external pressure,” *J. Fluid Mech.* **825**, 922–960 (2017).
- [60] J. M. Davis and S. M. Troian, “On a generalized approach to the linear stability of spatially nonuniform thin film flows,” *Phys. Fluids* **15**, 1344–1347 (2003).
- [61] S. Symon, K. Rosenberg, S. T. M. Dawson, and B. J. McKeon, “On non-normality and classification of amplification mechanisms in stability and resolvent analysis,” *Phys. Rev. Fluids* **3**, 053902 (2018).
- [62] M. Heil and O. E. Jensen, “Flows in deformable tubes and channels: Theoretical models and biological applications,” in *Flow Past Highly Compliant Boundaries and in Collapsible Tubes*, Fluid Mechanics and Its Applications, Vol. 72, edited by P W Carpenter and T J Pedley (Springer, 2003) pp. 15–49.
- [63] T. J. Pedley and D. Pihler-Puzović, “Flow and oscillations in collapsible tubes: Physiological applications and low-dimensional models,” *Sādhanā: J. Indian Acad. Sci.* **40**, 891–909 (2015).
- [64] E. Kaya, E. Aulisa, A. Ibragimov, and P. Seshaiyer, “A stability estimate for fluid structure interaction problem with non-linear beam,” in *Proceedings of the 7th AIMS International Conference*, Dynamical Systems and Differential Equations (DCDS), edited by X. Hou, X. Lu, A. Miranville, J. Su, and J. Zhu (Arlington, Texas, USA, 2009) pp. 424–432.
- [65] E. Aulisa, A. Ibragimov, and E. Y. Kaya-Cekin, “Fluid structure interaction problem with changing thickness beam and slightly compressible fluid,” *Discr. Contin. Dynam. Syst. Ser. S* **7**, 1133–1148 (2014).
- [66] I. Chueshov, E. H. Dowell, I. Lasiecka, and J. T. Webster, “Nonlinear elastic plate in a flow of gas: Recent results and conjectures,” *Appl. Math. Opt.* **73**, 475–500 (2016).
- [67] E. Boyko, M. Bercovici, and A. D. Gat, “Viscous-elastic dynamics of power-law fluids within an elastic cylinder,” *Phys. Rev. Fluids* **2**, 073301 (2017).
- [68] S. B. Elbaz and A. D. Gat, “Dynamics of viscous liquid within a closed elastic cylinder subject to external forces with application to soft robotics,” *J. Fluid Mech.* **758**, 221–237 (2014).
- [69] F. Gay-Balmaz, D. Georgievskii, and V. Putkaradze, “Stability of helical tubes conveying fluid,” *J. Fluids Struct.* **78**, 146–174 (2018).
- [70] R. Anoop and A. K. Sen, “Capillary flow enhancement in rectangular polymer microchannels with a deformable wall,” *Phys. Rev. E* **92**, 13024 (2015).
- [71] J. Bico, É. Reyssat, and B. Roman, “Elastocapillarity: When surface tension deforms elastic solids,” *Annu. Rev. Fluid Mech.* **50**, 629–659 (2018).
- [72] G. Hou, J. Wang, and A. Layton, “Numerical methods for fluid-structure interaction — A review,” *Commun. Comput. Phys.* **12**, 337–377 (2012).
- [73] E. Jones, T. Oliphant, P. Peterson, and Others, “SciPy: Open source scientific tools for Python,” GitHub (2001).
- [74] J. H. Ferziger and M. Peric, *Computational Methods for Fluid Dynamics*, 3rd ed. (Springer-Verlag, New York, 2002).
- [75] P. J. Roache, *Verification and Validation in Computational Science and Engineering* (Hermosa Publishers, Socorro, New Mexico, 1998).

Appendix A: Numerical details

To summarize, Eq. (5) is the time-stepping equation of the FSI, while Eqs. (19), (16) and (18) are used to calculate the pressure P iteratively. The construction of accurate and stable method for such two-way coupled FSIs is generally a difficult problem (see, e.g., [72] and the references therein). The scheme described below is based on a segregated solver, which was implemented in Python, making use of the routines from SciPy [73]. In this section, for brevity, we denote the displacement U_Y by U , without fear of confusion.

1. Create mesh (uniform grid of N_X points on the domain $[0, 1]$ with nodes $X_j = j\Delta X$, $\Delta X = j/(N_X - 1)$, $j = 0, \dots, N_X - 1$) and the appropriate sparse matrices corresponding to the spatial derivative operators.
2. Initialize by setting ($\forall j$): $Q^\star = Q^{n+1} = Q^n = Q^{n-1} = 1$; $H^\star = H^{n+1} = H^n = H^{n-1} = 1$; $U^\star = U^{n+1} = U^n = U^{n-1} = 0$; $P = 0$. A superscript of n , $(n - 1)$ and \star denotes values at the current time step, the previous time step, and at the intermediate (sub-time-step) iteration stage, respectively.
3. Start the time loop from $n = 0$ and preform N_T time steps with fixed time step ΔT , to the final selected time.
4. Start inner iteration loop to determine Q^\star and resolve the nonlinearity.
5. Solve for pressure from Eq. (18) by discretizing the time and space derivatives and rewriting the equation as a definite integral for the pressure:

$$P(X, T) - P(1, T) = \int_1^X \left[-\frac{\epsilon Re St}{H^\star} \left(\frac{4Q^\star - 4Q^n + Q^{n-1}}{2\Delta T} \right) - \frac{6 \epsilon Re}{5 H^\star} \left\{ \mathbf{D}_1 \left[\frac{(Q^\star)^2}{H^\star} \right] \right\} - \frac{12Q^\star}{(H^\star)^3} \right] dX, \quad (\text{A1})$$

which is subject to the outlet boundary condition: $P(1, T) = 0$. Here, \mathbf{D}_1 is a discrete spatial operator corresponding to $\partial/\partial X$ constructed with second-order central-difference schemes (CDS) [74].

A custom integration loop is used to obtain $P(X_j, T)$. Specifically, the values of the integral over every grid cell, i.e., $\int_{X_j}^{X_{j+1}} \dots dX$, which we term a ‘‘sub-integral,’’ is pre-calculated. Then, to evaluate $P(X_j, T)$ at a particular node j , the appropriate set of sub-integrals are added together. This results in significant computational cost savings as compared to using a built-in integration routine that recalculates the whole integral for each j .

6. Solve for U^* via Eq. (5), which is discretized fully-implicitly with second-order CDS for the second-order time derivative, yielding a standard matrix equation formulation:

$$\left\{ \mathbf{D}_4 - \alpha(\mathbf{D}_1[U^*])^2 \mathbf{D}_2 + \frac{1}{(\Delta T)^2} \mathbf{I} \right\} U^* = -\frac{1}{(\Delta T)^2} (-2U^n + U^{n-1}) + P. \quad (\text{A2})$$

\mathbf{D}_4 , \mathbf{D}_2 , \mathbf{D}_1 are the discrete fourth, second and first spatial differentiation matrices constructed using second-order CDS, appropriately modified for the present boundary conditions. \mathbf{I} is the $N_X \times N_X$ identity matrix. Equation (A2) is solved using `spsolve` from the linear algebra libraries in SciPy [73].

U^* is a temporary variable used during the internal (sub-time-step) iterations to get a fully-implicit scheme for stable loading of the beam. If necessary, U^* can be under-relaxed:

$$U^* = \omega U^* + (1 - \omega) U^{n+1}, \quad (\text{A3})$$

where $\omega \in (0, 1]$ is the *relaxation factor*.

7. Update H^* from U^* via Eq. (19).
8. Find Q^* by solving Eq. (16), which can again be re-cast as a definite integral from 0 to X , and after discretizing the time derivative becomes:

$$Q^*(X, T) - Q(0, T) = -St \int_0^X \left(\frac{3H^* - 4H^n + H^{n-1}}{2\Delta T} \right) dX, \quad (\text{A4})$$

where $Q(0, T) = 1$ is the flow rate at the inlet given by the boundary condition.

9. Update the inner iteration. To ensure that the both the solid and fluid solutions have independently converged, the residual is calculated as:

$$r = \max \left\{ \frac{\max_j |U^* - U^{n+1}|}{\max_j |U^{n+1}|}, \frac{\max_j |P - P^{n+1}|}{\max_j |P^{n+1}|} \right\}, \quad (\text{A5})$$

and a tolerance of 10^{-6} is used for the residual convergence criterion after testing tolerance values ranging from 10^{-4} to 10^{-8} . As we never use values stored in the $(n + 1)$ variables, they can be used as containers for old values of the \star variables, which simplifies the definition of r above.

Iterating on U^* causes the values of Q^* and H^* to change, which results in changes in P . So, the beam bending equation is our main time-stepping equation and P is our nonlinear loading that requires internal iterations to obtain a stable scheme. While iterating on P , all of U^n , U^{n-1} , H^n , H^{n-1} , Q^n and Q^{n-1} are known and constant. Set $(\forall j)$: $U^{n+1} = U^*$, $H^{n+1} = H^*$, $Q^{n+1} = Q^*$.

10. Update (external) time-stepping loop by setting $(\forall j)$: $U^{n-1} = U^n$, $U^n = U^{n+1}$; $H^{n-1} = H^n$, $H^n = H^{n+1}$; $Q^{n-1} = Q^n$, $Q^n = Q^{n+1}$.

The discrete spatial operators were verified to be second-order accurate by applying them to smooth test functions. The second-order accuracy of the whole time-stepping algorithm was verified by setting up test cases for the solid mechanics problem (no flow) and the coupled-problem (prescribed wall motion generating flow) for which exact solutions were calculated via the *method of manufactured solutions* [75]. A mesh size and time step independence study was carried out before selecting a ΔT ; for further details, see [49].

For homogeneous boundary conditions, the same stencil can be used for the boundary points (as that used away from the boundary points on the grid) when defining \mathbf{D}_1 , \mathbf{D}_2 and \mathbf{D}_4 . Specifically, this re-use of the stencil can be accomplished by omitting weights that falls on the boundary points’ neighbors outside the boundary. For example, in case of \mathbf{D}_2 formed by CDS, the first row will have $-2/(\Delta X)^2$, $1/(\Delta X)^2$ as its entries in first and second column, omitting the weight $1/(\Delta X)^2$ that would be applied to the left-hand ($j = -1$) neighbor.